Journal of The Electrochemical Society

Solution Synthesis of Sb_2S_3 and Na_3SbS_4 Solid-State Electrolyte

Journal of The Electrochemical Society, 2021 **168** 110533
1945-7111/2021/168(11)/110533/8/$40.00 © 2021 The Electrochemical Society ("ECS"). Published on behalf of ECS by IOP Publishing Limited

Solution Synthesis of Sb_2S_3 and Na_3SbS_4 Solid-State Electrolyte

Saeed Ahmadi Vaselabadi, William H. Smith, and Colin A. Wolden[z]

Department of Chemical and Biological Engineering, Colorado School of Mines, Golden, CO, United States of America

Sodium thioantimonate (Na_3SbS_4) is an attractive solid-state electrolyte for sodium-ion batteries due to its high ionic conductivity and stability in protic solvents. Herein, we describe solution-based routes for its synthesis. First, we demonstrate the synthesis of the Sb_2S_3 precursor via thermodynamically favorable metathesis between Na_2S and $SbCl_3$. This solution-based approach is further extended to couple the resulting Sb_2S_3 with Na_2S for the synthesis of Na_3SbS_4. It is shown that ethanol is a superior solvent to water for solution-based synthesis of Na_3SbS_4 with respect to yield, morphology, and performance. Amorphous Sb_2S_3 synthesized from low-temperature metathesis produced highly crystalline Na_3SbS_4 with a room temperature Na^+ conductivity of 0.52 mS cm^{-1} and low activation energy, comparable to leading values reported in the literature.
 [DOI: 10.1149/1945-7111/ac3752]

Manuscript submitted August 12, 2021; revised manuscript received October 20, 2021. Published November 18, 2021.

Supplementary material for this article is available online

Sodium-ion batteries are attractive for low-cost energy storage necessary to manage fluctuations in renewable electricity due to sodium's abundance, low cost, and reduced Environ. impact relative to their high-performance lithium counterparts.[1–4] Replacement of the organic liquid electrolyte with a thin solid-state electrolyte (SSE) can further enhance performance and specific capacity. Moreover, the use of SSEs improves reliability by preventing safety concerns such as flammability and leakage. Among various classes of SSEs, sulfides have received significant attention in the research community due to their high ionic conductivity (> 0.1 mS cm^{-1}) as well as their ability to efficiently contact electrodes based on their deformability.[5–7] Synthesis of cubic Na_3PS_4 via ball-milling with a conductivity of 0.2 mS cm^{-1} was the starting point in the development of highly conductive chalcogenide-based sodium conductors.[8] Since then, extensive research has led to development of new SSEs in NPS class such as Na_3PSe_4 (1.16 mS cm^{-1}),[9] $Na_{2.9375}PS_{3.9375}Cl_{0.0625}$ (1 mS cm^{-1}),[10] $Na_3P_{0.62}As_{0.38}S_4$ (1.46 mS cm^{-1}),[11] and $Na_{2.730}Ca_{0.135}PS_4$ (~1 mS cm^{-1}).[12]

A drawback of thiophosphates' is their reactivity that requires extra handling considerations such as the need of air-free environment that manifest by increasing the production costs. The phosphorus cation typically reacts with oxygen and water vapor in ambient air and release toxic H_2S gas. Hard and soft acid and base (HSAB) theory suggests that substitution of P^{5+} with a softer acid such as Sb^{5+} would minimize this undesired reaction.[13,14] As a result, antimony-based electrolytes such as sodium thioantimonate (Na_3SbS_4) have been proposed as an air-stable solid electrolyte with achievable conductivity of more than 1 mS cm^{-1}. The tetrathioantimonate (SbS_4^{4-}) group is stable in presence of moisture because of the strong bonding between Sb^{5+} and S^{2-}. As such, Na_3SbS_4 can withstand water and other protic solvents while maintaining high ionic conductivity.[13–15]

Sulfide-based SSEs are often synthesized through high-temperature reactions between solid-state precursors conducted in quartz ampoules followed by ball-milling, which is energy and time intensive. This has prompted the development of solution-based synthesis approaches that offer low thermal budgets and are more amenable for scaleup for the synthesis of both binary precursors and compound SSEs.[16–18] Yoon et al.[13] reported the dissolution-precipitation synthesis of Na_3SbS_4 through producing the SSE via solid-state reaction at high temperatures as the first step. Next, Na_3SbS_4 was dissolved in solvents such as water and methanol and recrystallized while retaining a high ionic conductivity (0.1–0.3 mS cm^{-1}) proving its scalable solution processability. Furthermore, the same group demonstrated the aqueous synthesis of Na_3SbS_4 from binary metal sulfide precursors. SSE recovery was performed through an extra step of acetone addition as an anti-solvent (0.21 mS cm^{-1}) or ethanol wash of the vacuum-dried solution (0.15 mS cm^{-1}) followed by mild thermal annealing. The formation of toxic H_2S during the recovery process was examined as a drawback of this approach.[15] Tatsumisago et al.[19] also followed a similar aqueous route while 2-propanol was used as the anti-solvent. High conductivity of 1.2 mS cm^{-1} was achieved through a series of drying, pelletizing, and further annealing processes at a relatively high fabrication pressure (720 MPa).

In the case of Na_3SbS_4, the key binary precursors are sodium sulfide (Na_2S) and antimony trisulfide (Sb_2S_3). Our group recently described protocols for upgrading low-cost, technical grade sodium hydrate flakes into anhydrous Na_2S powder of exceptional purity.[17] Sb_2S_3 is a precursor to many thioantimonates SSEs based on sodium and lithium cations.[19,20] It has also been employed directly as an anode due to its high theoretical capacity (946 $mAhg^{-1}$).[21–23] Moreover, antimony trisulfide is a material of interest for solar energy conversion including thin film solar cells and photoelectrochemical water splitting.[24–26]

Solution chemistry approaches reported to date for Sb_2S_3 synthesis include chemical bath deposition (CBD)[27,28] and solvothermal[29–33] methods. CBD is typically employed to form thin films of metal sulfides used in photovoltaic applications. In a typical CBD procedure antimony trichloride ($SbCl_3$) and sodium thiosulfate ($Na_2S_2O_3$) precursors are combined in a solution of acetone and water, and CBD needs to be performed at low temperatures (<10 °C) to avoid the immediate precipitation of products.[28] Solvothermal methods also combine antimony salt (i.e., $SbCl_3$) with a sulfur source such as $Na_2S.9H_2O$,[29] Na_2S,[33] $Na_2S_2O_3{\cdot}5H_2O$,[30] and L-cysteine,[32] elemental sulfur[31] reacted in different solvents. However, this method requires the use of an autoclave at high pressure and temperature for a prolonged time to complete the formation of crystalline Sb_2S_3. In addition, a co-solvent like acetone[27] and ethylene glycol[33] is normally needed to buffer the undesired hydrolyses.

In this work, we demonstrate the formation of phase pure Sb_2S_3 via a simple metathesis reaction between antimony trichloride and sodium sulfide. Subsequently, the synthesized Sb_2S_3 is converted to Na_3SbS_4 via liquid-state reaction to validate the applicability that produces ionic conductivities ($\sigma = 0.52$ mS cm^{-1}) comparable with reported literature (Table I).[15,19] Previous solution-based synthesis of Na_3SbS_4 employed aqueous solution followed by an ethanol wash.[15] It is shown that use of ethanol simplifies the process, increases the yield, improves morphology and electrolyte performance. The composition and morphology of Sb_2S_3 and Na_3SbS_4 produced in this work are extensively characterized using a variety of techniques (XRD, TGA/DSC, Raman spectroscopy, TOF-SIMS, SEM-EDX) and correlated with ion conductivity measurements using impedance spectroscopy.

[z]E-mail: cwolden@mines.edu

Table I. Summary of Na_3SbS_4 synthesis parameters and performance reports in the literature.

Synthesis method	Solvent	Co-solvent	Precursors	T_{rxn} (°C)	T_{dry} (°C)	T_{an} (°C)	P_{fab} (MPa)	Blocking ion contacts	P_{stack} (MPa)	σ_{Na+} (mS/cm)	E_a (eV)	References
Hydrate Purification	—	—	$Na_3SbS_4.9H_2O$	RT	150	—	320	C-coated Al foils	—	1.05	0.22	14
Solid-state	—	—	Na_2S★, Sb_2S_3★, S✹	RT	—	550	370	Ti	—	1.10	0.20	13
Dissolution-precipitation	MeOH	—	Na_2S★, Sb_2S_3★, S✹	RT	100	—	370	Ti	—	0.23	0.37	
	H_2O	—								0.26	0.32	
Solution	H_2O	Ethanol	Na_2S★, Sb_2S_3★, S✹	RT	200	—	370	Ti	75	0.15	0.35	15
		Acetone								0.21	0.27	
Solution	H_2O	2-propanol	Na_2S▲, Sb_2S_3★, S★	80	150	—	720	Au	—	0.95	0.24	19
Solution				80	150	100				1.20	0.24	
Solution	H_2O	Ethanol	$Na_2S.9H_2O$❋, Sb_2S_3✹, S✹	RT	140	—	350	In foils	—	0.12	—	34
Solution	ACN	—	Na_2S❋, Sb_2S_3❋, S❋	50	80	450	240	Carbon paste	—	0.25	0.30	35
Solution	H_2O	Ethanol	Na_2S■, Sb_2S_3■, S★	RT	140	—	240	Stainless Steel	120	0.33	0.14	This work
	Ethanol	—								0.52	0.13	

★ Sigma Aldrich, > 99.5%, ✹ Alfa Aesar, > 99.5%, ▲ Nagao Co,, 99.1%, ❋Aladdin, 99.99%, ■ In-house synthesis.

Experimental

Materials.—Sodium sulfide hydrate flakes (60%, Sigma Aldrich) were converted to anhydrous Na_2S and purified using the dehydration/H_2 reduction procedure described in the literature.[17] $SbCl_3$ (99+%, Alfa Aesar) and elemental sulfur (S, Sigma Aldrich, 99.998% trace metal basis) were used as received. Solvents employed included DI water, methanol (MeOH, Sigma-Aldrich, anhydrous, 99.8%), and ethanol (Ethanol, Sigma Aldrich, anhydrous, ⩾99.5%). Ambients employed for various evaporation and annealing processes included vacuum evacuated tube furnace, UHP grade argon, or a 10% H_2S/Ar specialty gas mixture (Matheson).

Characterization.—Thermogravimetric analysis and differential scanning calorimetry (TGA/DSC) was performed on a TA Instruments SDT-Q600 model. For a typical run, 10 mg of sample was loaded into a pre-cleaned alumina pan and heated under flowing Ar from RT to 600 °C at 10 °C min^{-1} rate and then cooled down naturally. X-ray diffraction (XRD) was performed with a Philips X'Pert X-ray diffractometer with Cu Kα radiation ($\lambda = 0.15405$ nm) between 10 and 60° at a scan rate of 2–5° min^{-1}. Samples were prepared on a glass slide with a protective tape covering the material to prevent undesired reactions with ambient air. XRD background subtraction was performed using HighScore software. Confocal Raman spectroscopy was performed with a WiTec Alpha300 laser confocal microscope equipped with a Raman spectrometer. The samples were prepared by placing 0.1 mm glass covers on powder samples secured on glass slides. Spectragryph software was used to subtract the Raman background.

Fourier-transform infrared spectroscopy (FTIR) was performed with a Nicolet Summit FTIR spectrometer using an attenuated total reflection (ATR) accessory equipped with a diamond crystal. Field emission scanning electron microscopy (FESEM) images were collected on a JEOL JSM-7000F FESEM instrument equipped with energy-dispersive X-ray spectroscopy (EDX) for compositional analysis. To prepare the samples for SEM and EDX measurements, powder samples were immobilized onto an aluminum stub by using a double-sided carbon tape. An accelerating voltage of 5 kV was used for taking the SEM image while a higher voltage of 12–25 V was employed for EDX spectra collection. Compositional analysis was performed on Na_3SbS_4 pellets using time of flight secondary ion mass spectrometry (TOF-SIMS, IONTOF.SIMS 5). The TOF-SIMS sputter parameters were 0.5 keV and 1.17 × 10 Cs^+ cm^{-2} on a 400 * 400 μm^2 scanning area for depth profiling. All sample preparation was done in an Ar glovebox, though samples were briefly exposed to ambient upon transfer to various characterization instrumentation.

Pellets of Na_3SbS_4 SSE were prepared for conductivity measurement via conventional uniaxial pressing. For this purpose, 150–250 mg of the electrolyte was loaded into a PEEK split cell with 12 mm diameter, and pellets 0.9–1.1 mm in thickness were formed by cold pressing using a hydraulic press (YLJ-15L, MTI Corp.). The electrolyte powders were pressed gradually by increasing pressure in 60 MPa increments (30-second stabilization interval) and finally were held for 5 min at the target pressure of 240 MPa (P_{fab}). After reducing the pressure to zero, different stack pressure (P_{st}) was applied to the pellet for 2 min. The SSE pellets were contacted using stainless steel plungers as the ion-blocking electrodes for electrochemical characterization. A Gamry Interface 1000E potentiostat was used to perform electrochemical impedance spectroscopy (EIS) measurements across a frequency range of 1 Hz to 1 MHz. Temperature-dependent measurements were performed by contacting the cell assembly with a temperature-controlled heating coil connected to a PID controller. DC polarization measurements were performed by applying three step potentials (0.5, 0.75, and 1 V) to the sample and recording the transient current. The steady-state current was recorded after 2 h at each step potential, and the electrical conductivity was calculated using Ohm's law.

Results and Discussion

Metathesis of Sb_2S_3.—Metathesis is a simple chemical process that involves counterion exchange between two chemical species

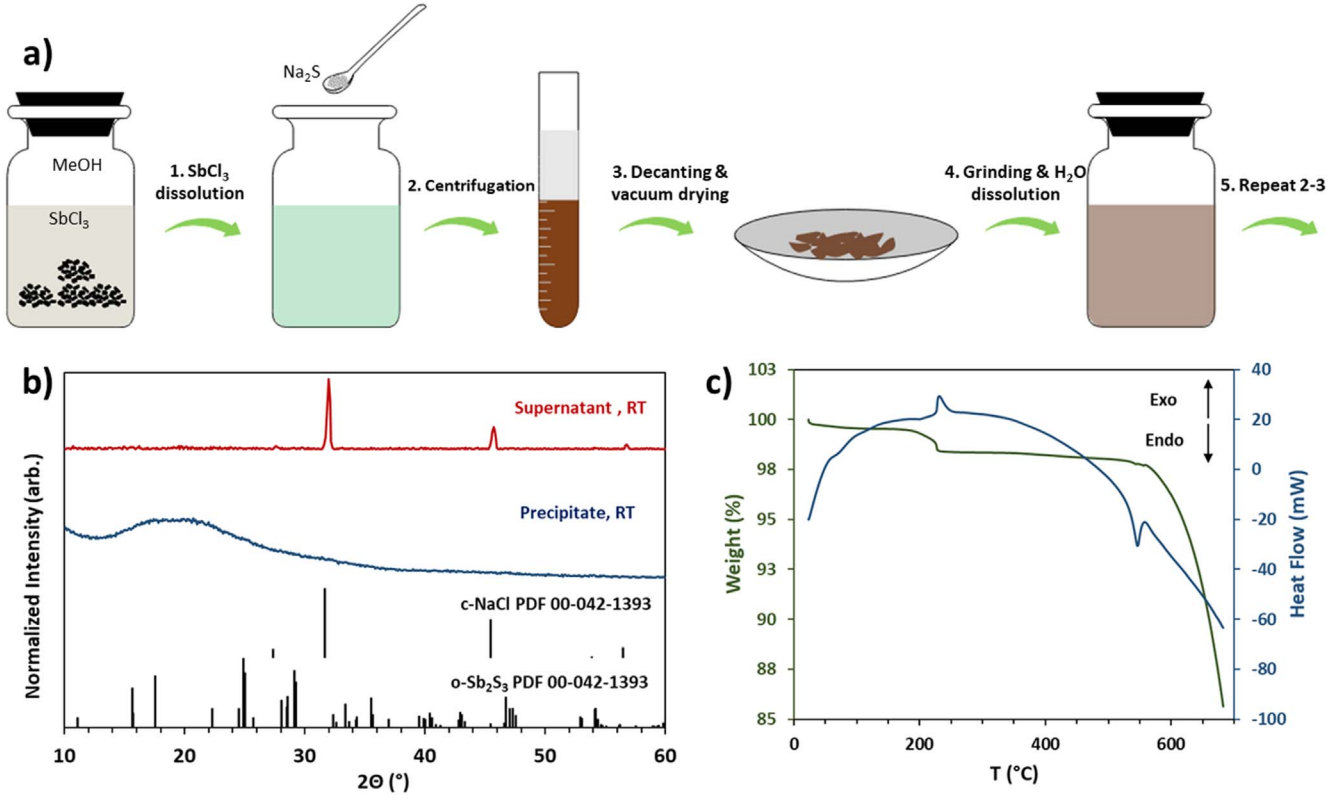

Figure 1. (a) Schematic illustrating the Sb_2S_3 synthesis procedure in methanol, (b) XRD patterns of the metathesis precipitate and supernatant, (c) TGA/DSC traces of Sb_2S_3 recovered from methanol.

where one of the products often precipitates, providing favorable energetics. The salts employed are typically low cost and widely available. The first reaction of interest is the thermodynamically favorable metathesis reaction between Na_2S and $SbCl_3$:[36,37]

$$3Na_2S_{(sol)} + 2SbCl_{3(sol)} \rightarrow Sb_2S_{3(s)} + 6NaCl_{(sol)},\ \Delta G^\circ = -1160.2\ \text{kJ mol}^{-1} \quad [1]$$

One of the important aspects of metathesis is appropriately choosing a solvent that both facilitates the reaction kinetics and acts as a separation medium for the resulting products. Also, the potential of side reactions between the solvent and precursors can play an important role in the formation of impurities. For instance, some metal sulfides may get hydrolyzed with protic solvents. While $SbCl_3$ is moisture sensitive and needs to be handled in an air-free environment, its full dissolution in the solvent is the driving force for the metathesis reaction. As highly polar H_2O causes hydrolysis of the starting precursor, we chose methanol as the reaction solvent that provides both high precursor solubility as well as acceptable separation access for both Sb_2S_3 and NaCl products. NaCl is expected to remain fully dissolved in methanol while sparingly insoluble Sb_2S_3 will precipitate.

Figure 1a demonstrates the procedure used for metathesis reaction of Sb_2S_3: First, $SbCl_3$ was dissolved in MeOH forming a 0.4 M solution that was allowed to equilibrate at room temperature. A stoichiometric amount of a 0.6 M Na_2S solution was added gradually. The solution color turned brown instantaneously upon Na_2S addition indicating fast reaction kinetics, though the mixture was stirred for one day to ensure the reaction went to completion. The dark brown solution was centrifuged and decanted. The precipitate was washed initially with MeOH. The precipitate and supernatant were dried at room temperature under vacuum. An extra step of grinding for 5 min in a pestle and mortar and H_2O washing was added to ensure the full separation of metathesis products. Figure 1b displays the XRD patterns of the Sb_2S_3 metathesis precipitate and solids recovered from the supernatant. The precipitate is amorphous with no discernable crystalline features while the solids recovered from the supernatant match the cubic phase of NaCl. The extra grinding and H_2O washing were required as XRD patterns of the precipitate after just the MeOH wash contained residual NaCl (Fig. S1a available online at stacks.iop.org/JES/168/110533/mmedia). The precipitate composition was analyzed using EDX, which supported the formation of Sb_2S_3. EDX analysis found a S/Sb ratio of ~1.3–1.4 that is very close to the ideal value of 1.5 considering the uncertainties in this technique (Fig. S1b).

Figure 1c displays TGA/DSC scans of amorphous Sb_2S_3 to identify possible crystallization points. The heat trace shows a weak exothermic peak at ~233 °C coincided with ~1.5% weight loss. The slight weight reduction might correspond to the volatilization of compounds with excess sulfur such as polysulfides. The identified crystallization temperature is in good agreement with the reported temperature for the thermal activation of Sb_2S_3 thin films.[27] The TGA trace indicates that Sb_2S_3 is thermally stable before reaching its melting point at ~550 °C.[38–40]

Annealing in the presence of elemental sulfur[41] and H_2S[42] have been shown to improve the crystallinity of metal sulfides, and the use of H_2S especially provides a well-controlled and reproducible annealing process by avoiding the difficulties of handling sulfur. The Sb_2S_3 powder was annealed at 200, 250, and 300 °C using a packed bed setup under flowing of 10% H_2S/Ar gas mixture (40 sccm) in a tube furnace at reduced pressure (~70 torr). The XRD patterns of the thermally annealed Sb_2S_3 (Fig. 2a) samples demonstrate significant crystalline phase with diffraction peaks matching those for an orthorhombic structure with Pnma (62) space group (PDF 01–070–9254).[28] As manifested by more intense Bragg peaks, increasing the temperature improves the degree of crystallinity. Annealing under Ar flow at 250 °C also showed a similar degree of crystallinity in comparison to H_2S-annealed Sb_2S_3 (Fig. S2). Figure 2b shows the Raman spectra of the annealed Sb_2S_3 that further confirms the presence of Sb_2S_3. As described in detail by Parize and coworkers.,[27] the onset of crystallization at 200 °C has coincided with the formation of weak broad peaks centered at 280 and 310 cm^{-1} while further increasing the temperature solidifies the crystallization process and gives rise to more characteristic peaks corresponding to Sb_2S_3. A minor formation of residual senarmontite Sb_2O_3 was observed in Raman spectra as the annealing temperature increased. The characteristic peaks corresponding to Sb–S bonds are observed at ~190, ~240, ~285, and ~310 cm^{-1}.[26,27]

To investigate the impact of Na_2S reagent purity on Sb_2S_3 products, Sb_2S_3 was synthesized following the same procedure using technical grade Na_2S ($Na_2S.xH_2O$, x~3) that contains 40% water. Figure S3 displays the FTIR spectra of resulted Sb_2S_3 from purified and hydrated Na_2S reagent dried at room temperature without further processing. Sb_2S_3 derived from purified Na_2S exhibits a lower level of impurity. The main peaks include symmetric stretching band[43] of SO_3^{2-} and residual water remaining (O–H bending and stretching modes at 1570 and 3200 cm^{-1}, respectively).[44] Further drying can desolvate the residual water to improve the Sb_2S_3 impurity profile. On the other hand, Sb_2S_3 derived from hydrated precursors mainly carries on the insoluble impurities already present in the sodium sulfide such as oxysulfurs (Na_2SO_x) and residual carbon bindings.[17] Detailed descriptions of the observed impurity peaks are summarized in Table SI. These results confirm that the presence of impurities in the Na_2S reagent can negatively affect the functionality of the sulfide product.

Solution synthesis of Na_3SbS_4.—Synthesized Sb_2S_3 was then used as a reagent with Na_2S to form Na_3SbS_4 SSEs using both water and ethanol solvents. First, Na_3SbS_4 was synthesized by mixing Sb_2S_3, Na_2S, and elemental sulfur in an aqueous solution following the procedure described by Yoon and coworkers.[15] After mixing water was evaporated at 140 °C and the recovered powder was washed with ethanol multiple times to remove any unreacted precursors and further vacuum dried at room temperature to produce a light green powder (Fig. S4). The following mechanism was suggested for the formation of Na_3SbS_4 in aqueous solutions:

$$3Na_2S_{(s)} + 3H_2O_{(l)} \rightarrow 6Na^+_{(aq)} + 3HS^-_{(aq)} + 3OH^-_{(aq)} \quad [2]$$

$$Sb_2S_{3(s)} + HS^-_{(aq)} + OH^-_{(aq)} \rightarrow Sb_2S^{2-}_{4(aq)} + H_2O_{(l)} \quad [3]$$

$$Sb_2S^{2-}_{4(aq)} + 2HS^-_{(aq)} + 2OH^-_{(aq)} \rightarrow 2SbS^{3-}_{3(aq)} + 2H_2O_{(l)} \quad [4]$$

$$2SbS^{3-}_{3(aq)} + 2S_{(s)} \rightarrow 2SbS^{3-}_{4(aq)} \quad [5]$$

$$3Na_2S_{(s)} + Sb_2S_{3(s)} + 2S_{(s)} \rightarrow 2Na_3SbS_{4(s)} \quad [6]$$

The formation of the bisulfide anion (HS^-) is the key to driving this reaction; however, competition with the Na_2S hydrolysis pathway below compromises yield and releases H_2S:[45]

$$Na_2S_{(s)} + H_2O_{(l)} \rightarrow NaHS_{(aq)} + NaOH_{(aq)} \quad [7]$$

$$NaHS_{(aq)} + H_2O_{(l)} \rightarrow H_2S_{(g)} + NaOH_{(aq)} \quad [8]$$

Therefore, H_2S formation, as well as handling material losses, contribute to the low yield of Na_3SbS_4 synthesis in water. We hypothesized that ethanol would be a viable option for the single-step synthesis of Na_3SbS_4 that could minimize the H_2S formation due to its lower polarity and the insolubility of Na_3SbS_4 in ethanol.[15] Figure 3a displays the schematic of Na_3SbS_4 synthesis in ethanol. In this process, 0.075 M of Sb_2S_3, 0.15 M of elemental sulfur, and 0.450 M (twice the stoichiometric concentration) of Na_2S were dissolved in ethanol and stirred overnight to fully react. Extra

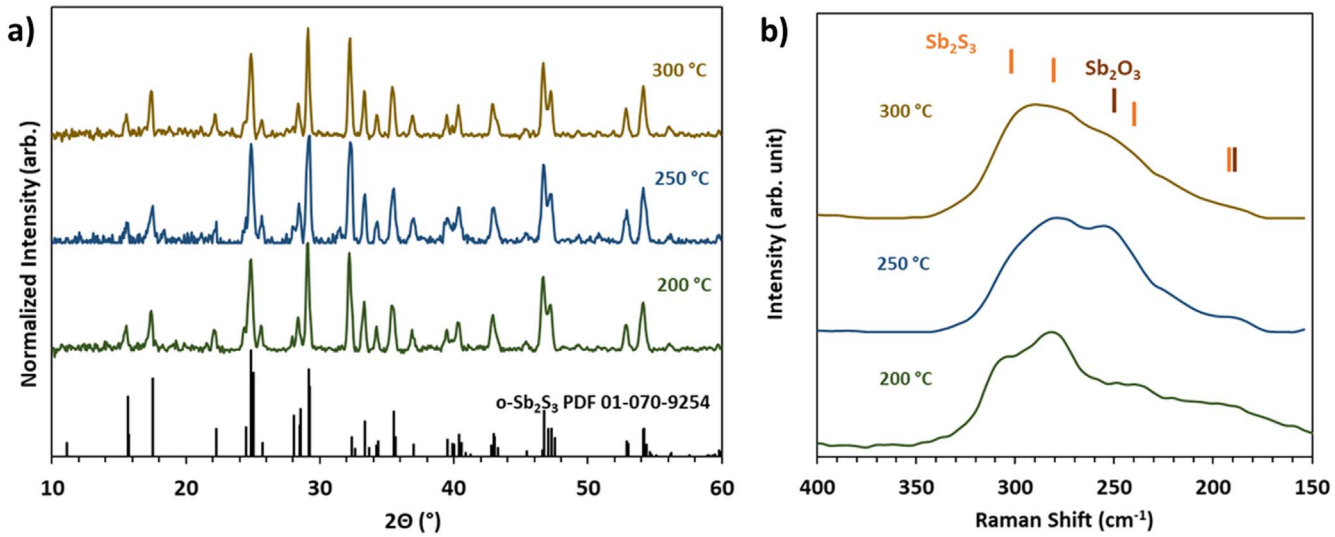

Figure 2. (a) XRD, and (b) Raman spectra of H_2S annealed Sb_2S_3.

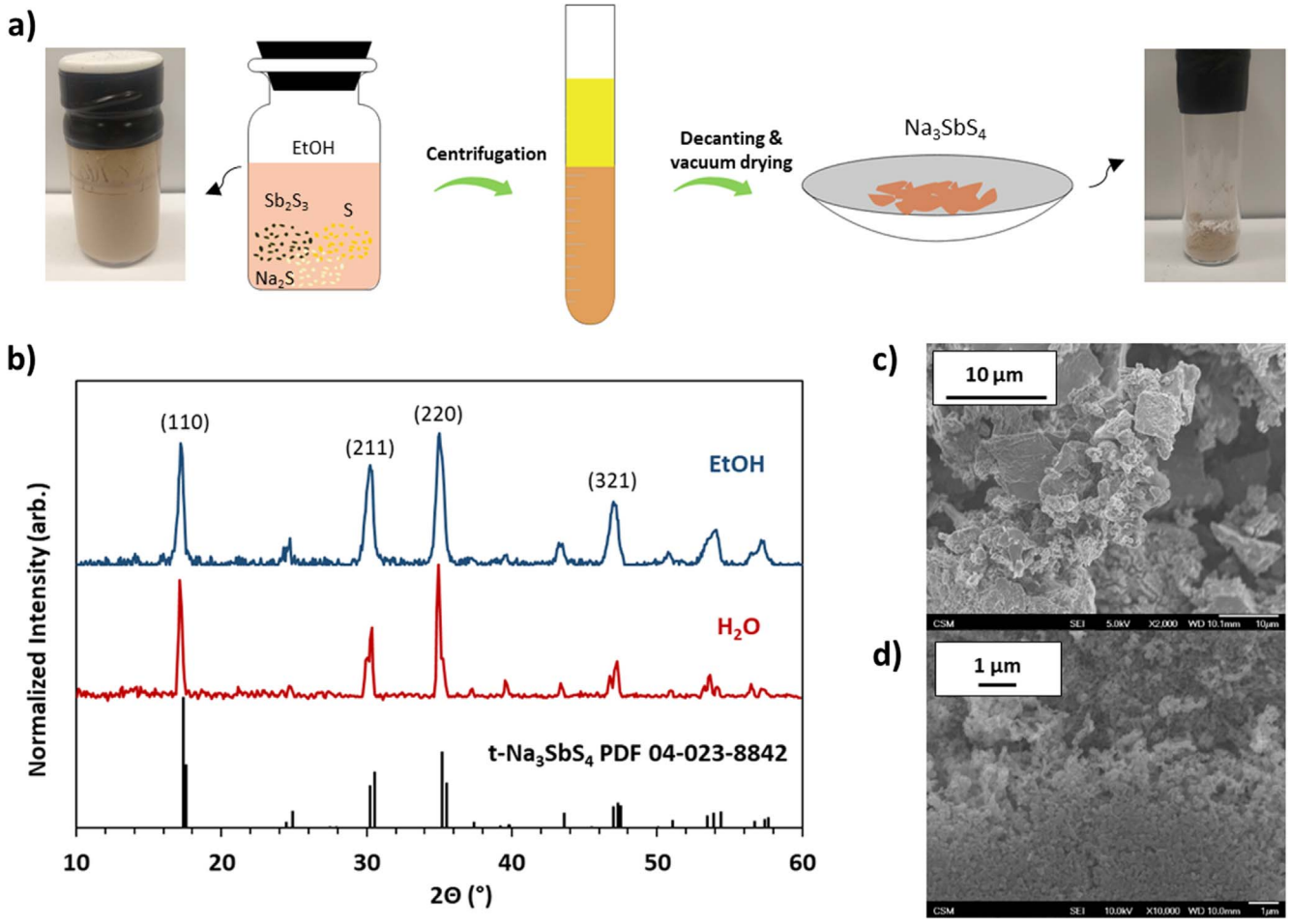

Figure 3. (a) Schematic illustrating the Na_3SbS_4 synthesis procedure in ethanol, (b) XRD patterns of Na_3SbS_4 recovered from methanol and water. SEM micrographs of Na_3SbS_4 recovered from (c) H_2O (2,000X), (d) ethanol (10,000X).

Na_2S was used to ensure the Sb_2S_3 consumption in the reaction.[15] To recover Na_3SbS_4, the solution was centrifuged and washed with ethanol several times. A light brown powder was obtained after vacuum drying the precipitate. The powder was further dried at 140 °C to remove any solvated complexes. The Na_3SbS_4 recovered from ethanol showed a near stoichiometric yield of 91% resulting in a significant improvement in recovery compared to the aqueous solution (~72%).

Figure 3b demonstrates the XRD patterns of the Na_3SbS_4 recovered from ethanol and water. Despite their color difference (Figs. 1a and S4), both ethanol and water products are highly crystalline with a tetragonal structure. Typically, it has been

observed that Na_3SbS_4 follows the powder pattern in which the (110) peak is most prominent. In this work for both ethanol and water, there is a degree of preferential orientation in the (211) and (220) directions. The ethanol-recovered Na_3SbS_4 exhibits broadened peaks with higher full-width half-maximum (FWHM) compared to sharp split peaks of the tetragonal phase from aqueous synthesis. The differences in FWHM are consistent with the morphology revealed by SEM. The SEM images of Na_3SbS_4 synthesized in the aqueous solution (Fig. 3c) features fairly large individual crystals ($\sim$1 micron) that also assemble into large agglomerates. In contrast, ethanol-derived SSE (Fig. 3d) displays uniform nanocrystals on the order of $\sim$100 nm. The difference in grain size is consistent with the observation of Scherrer broadening in the XRD patterns of the ethanol-derived Na_3SbS_4. Zhang et al.[46] reported production of tetragonal Na_3SbS_4 with less than 30 nm grain size and higher conductivity achieved through a ball-milling step followed by solid-state synthesis. On the other hand, Tatsumisago et al.[19] also showed that the solution approach creates a smaller grain size of Na_3SbS_4 ($< 1\ \mu$m) compared to the mechanochemical method; however, that could explain the lower ionic conductivity of the solution method due to the presence of a higher number of grain boundaries.

The composition of the two materials is compared in Fig. 4. Figure 4a shows the Raman spectra of Na_3SbS_4 samples recovered from ethanol and water. The observation of symmetric (ν_s = 368 cm^{-1}), and asymmetric (ν_a = 389, 409 cm^{-1}) stretching vibration peaks of SbS_4^{4-} confirms the formation of tetrathioantimonate anions in both samples. The attenuated peaks at 168 and 201 cm^{-1} are attributed to the deformational vibrations of SbS_4^{4-}, δ_F and δ_E, respectively.[47,48] Figure 4b displays the negative ion intensity profiles obtained from TOF-SIMS profiling of Na_3SbS_4 derived from both solvents as a function of sputter time. The signals from ethanol- and water-derived electrolytes are shown as blue and red, respectively. For the principal elements (Na, Sb, S) there is no discernible difference based on solvent. Although present in a 3:1:4 molar ratio the dramatic difference in intensity reflects each element's ability to form negative ions, which is why the intensity of electronegative S is more than 3 orders of magnitude greater than electropositive Na. The only discernible difference between the two materials is the level of the oxygen impurities, with ethanol-derived material containing about twice as much oxygen as water-derived material. Without standards, absolute values cannot be assessed but we note that oxygen is significantly more electronegative than sulfur, which is why its intensity is relatively high despite likely being present at levels less than 0.1%. The only other element detected was trace amounts of Cl that were present at identical levels for both solvents (not shown), presumably introduced during Sb_2S_3 metathesis (Fig. S1b). The profiles suggest that the surface may be slightly enriched with O, but this may be an artifact of sputter initiation or reflect contamination from sample transfer in air. The bulk composition appears homogeneous in both samples. Figure S5 shows the homogenous distribution of constituent atoms from the 3D TOF-SIMS profiles recovered from water and ethanol solutions.

To understand the difference in oxygen content TGA scans were performed of Na_3SbS_4 recovered from ethanol and water (Fig. S6). The H_2O-derived sample shows a very stable weight trace with no significant weight loss; however, the ethanol-recovered SSE displays a small weight loss at 62.5 °C that is attributed to the presence of ethanol solvated moieties. This is consistent with the differences in residual oxygen observed in TOF-SIMS. Annealing at higher temperatures with better control over the mass transfer of the solvent evaporation, in a fluidized regime, for instance, needs to be explored to fully eradicate the solvent impurities.

EIS measurements were performed to measure the ionic conductivity of Na_3SbS_4. Nyquist plots of various stacking pressure and their fitted curves are shown in Figs. 5a, 5b. The spectra were fitted with an equivalent circuit consisting of a parallel resistor (R1) and constant phase element (CPE1) arrangement that is in series with an additional CPE (CPE2).[49,50] The use of stainless steel blocking electrodes contributed significant contact resistance that was overcome through the application of stacking pressure. Stacking pressure helps with obtaining nominal conductivity values close to innate bulk values and ultimately decreases the chances of delamination during battery cycling operation.[51–53] All samples have been constructed by constant fabricated pressure of 240 MPa while stacking pressure is variant. Figure 5c shows the ionic conductivity of Na_3SbS_4 recovered from ethanol and water as a function of stacking pressure. For both solvents, pressure-induced contact during EIS measurement improves the conductivity before reaching a constant plateau at pressure more than 100 MPa. The conductivity of ethanol-derived Na_3SbS_4 was consistently greater than its aqueous counterparts by nearly a factor of 2. We speculate that the small improvement in conductivity of ethanol-derived Na_3SbS_4 is related to the homogenous, nanocrystalline morphology revealed in Fig. 3. Under compression we speculate that this morphology leads to lower

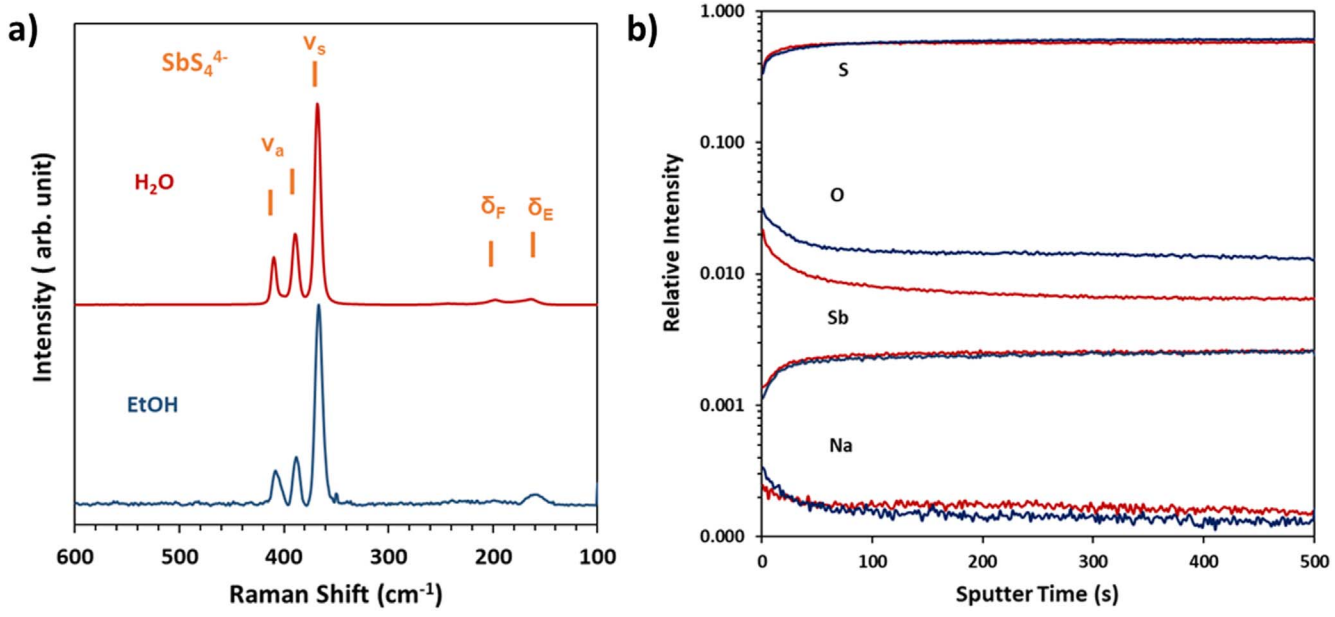

Figure 4. (a) Raman patterns, and (b) plot of negative ion intensities for selected elements from TOF-SIMS profiling of Na_3SbS_4 derived from ethanol (blue curves) and water (red curves).

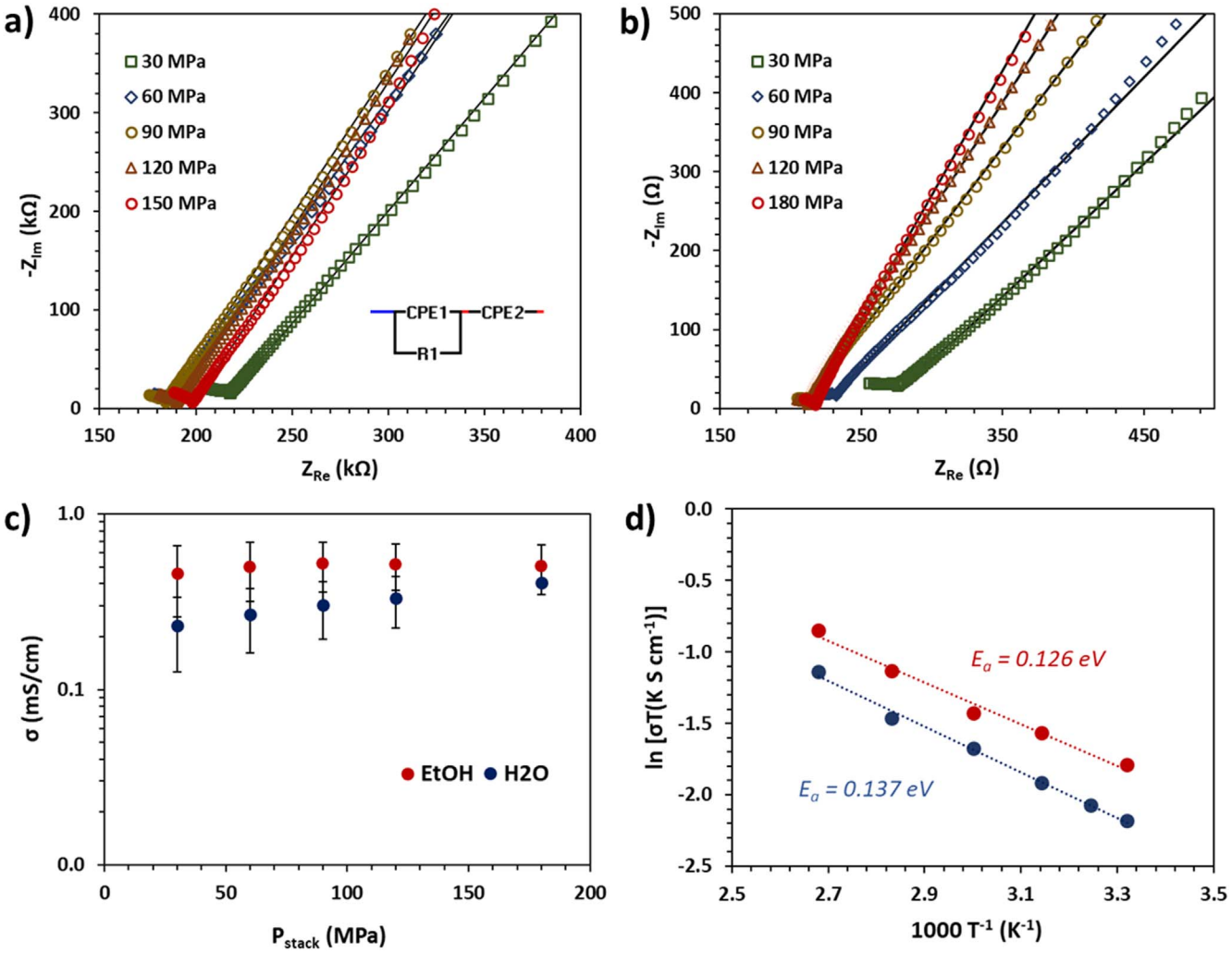

Figure 5. Nyquist plots and equivalent circuit used to fit data (inset) of Na_3SbS_4 recovered from (a) ethanol and (b) water solution at different stacking pressure; (c) the room temperature ionic conductivity of Na_3SbS_4 as a function of solvent and stacking pressure; (d) Arrhenius plots for the ionic conductivity of Na_3SbS_4 recovered from ethanol and water (P_{st} = 120 MPa).

porosity in the final pellet than is achieved with the larger, aggregated particles formed from water. Such a change would be expected to enhance deformability upon cold pressing and reduce grain boundary resistance and improve conductivity.[54–56]

To investigate the impact of Sb_2S_3 crystallinity on subsequent Na_3SbS_4 structure and functionality, Na_3SbS_4 was synthesized from both amorphous and crystalline Sb_2S_3 reagents in ethanol. The differences in crystallinity and conductivity were very minor (Fig. S7). This suggests that annealing of the Sb_2S_3 precursor is not required, and in fact amorphous Sb_2S_3 may be preferred for Na_3SbS_4 synthesis.

The Na_3SbS_4 synthesized from H_2O solvent achieved a room temperature ionic conductivity of σ_w = 0.33 mS cm^{-1} while the sample recovered from ethanol demonstrated a higher conductivity σ_e = 0.52 mS cm^{-1} (P_{st} = 120 MPa). The kinetics of Na^+ transport was investigated by performing temperature-dependent EIS. Figure 5a shows the Arrhenius plots of Na_3SbS_4 samples recovered from ethanol and water that fitted to the following equation:[50,57]

$$\sigma T = \sigma_0 e^{\left(-\frac{E_a}{RT}\right)} \quad [11]$$

The activation energy of Na^+ conduction calculated accordingly is ~0.14 eV for both synthetic routes, which is lower than previously reported values in the literature (Table I).[15,50]

The reasons for the lower activation energy are unclear. It may reflect the preferential orientation of the crystals (Fig. 3b) or the trace amounts of Cl, which has been correlated with lower activation energy in similar systems.[10] Figure S8 displays the Nyquist plots of Na_3SbS_4 recovered from ethanol and water solution at different temperatures. DC polarization measurements (Fig. S9) showed an insignificant electronic conductivity of 1.57*10^{-7} mS cm^{-1} which is 6 orders of magnitude lower than the recorded ionic conductivity.

Table I summarizes the findings of this work compared with the various reports in the literature. The conductivity achieved in this work using water is comparable or slightly higher than most solution-based reports, and the material derived from ethanol has the highest conductivity reported to date with the exception of the work of Tatsumisago et al.,[19] who employed extremely high pressure for pellet formation (720 MPa) as well as additional annealing treatments. The high conductivity achieved in this work may reflect the use of purified Na_2S, whose purity has been shown to be superior to commercial Na_2S[17] and this was reflected in the purity of the Sb_2S_3. The simplification of using a single solvent for synthesis and washing, the higher yield, mitigation of H_2S formation, improved morphology and higher conductivity clearly demonstrate the benefits of ethanol over water, which has been used exclusively for solution-based synthesis of Na_3SbS_4 to date.

Conclusions

This work reports a simple and scalable synthesis route to produce antimony trisulfide applicable for energy storage applications such as

sodium-ion battery anodes and as a precursor to solid-state electrolytes. XRD, EDX, and Raman corroborated the formation of amorphous Sb_2S_3 at room temperature, while H_2S annealing at a mild temperature of 250 °C resulted in a highly crystalline material. The utility of Sb_2S_3 was validated as a precursor reagent via solution synthesis of air-stable tetragonal Na_3SbS_4 with room temperature ionic conductivity of 0.52 mS cm^{-1}. It was shown that ethanol was the preferred solvent over water for this process, as it improves yield, mitigates hazardous byproducts, and delivers higher ionic conductivity. The findings of this work further prove the advantages of the reagent chemistry tuning in liquid-phase approaches that can be utilized for large scale fabrication of all-solid-state batteries.

Acknowledgments

This work was supported by the US National Sci. Foundation through Award 1825470 and an Advanced Industries grant from the Colorado Office for Economic Development and International Trade. We thank Dr. Michael Walker for conducting TOF-SIMS measurements employing instrumentation supported by the NSF MRI award 1726898.

ORCID

Colin A. Wolden https://orcid.org/0000-0001-6576-048X

References

1. H. Pan, Y. S. Hu, and L. Chen, *Energy Environ. Sci.*, **6**, 2338 (2013).
2. J. Y. Hwang, S. T. Myung, and Y. K. Sun, *Chem. Soc. Rev.*, **46**, 3529 (2017).
3. K. Kubota and S. Komaba, *J. Electrochem. Soc.*, **162**, A2538 (2015).
4. F. Wei, Q. Zhang, P. Zhang, W. Tian, K. Dai, L. Zhang, J. Mao, and G. Shao, *J. Electrochem. Soc.*, **168**, 050524 (2021).
5. Z. Zhang et al., *Energy Environ. Sci.*, **11**, 1945 (2018).
6. H. Jia, L. Peng, C. Yu, L. Dong, S. Cheng, and J. Xie, *J. of Mater. Chem. A*, **9**, 5134 (2021).
7. M. Li, C. Wang, Z. Chen, K. Xu, and J. Lu, *Chem. Rev.*, **120**, 6783 (2020).
8. S. Yubuchi, A. Hayashi, and M. Tatsumisago, *Chem. Lett.*, **44**, 884 (2015).
9. L. Zhang, K. Yang, J. Mi, L. Lu, L. Zhao, L. Wang, Y. Li, and H. Zeng, *Adv. Energy Mater.*, **5**, 1501294 (2015).
10. I. H. Chu, C. S. Kompella, H. Nguyen, Z. Zhu, S. Hy, Z. Deng, Y. S. Meng, and S. P. Ong, *Sci Rep.*, **6**, 1 (2016).
11. Z. Yu et al., *Adv. Mater.*, **29**, 1605561 (2017).
12. C. K. Moon et al., *ACS Energy Lett.*, **3**, 2504 (2018).
13. A. Banerjee, K. H. Park, J. W. Heo, Y. J. Nam, C. K. Moon, S. M. Oh, S.-T. T. Hong, and Y. S. Jung, *Angewandte Chem. - Int. Ed.*, **55**, 9634 (2016).
14. H. Wang, Y. Chen, Z. D. Hood, G. Sahu, A. S. Pandian, J. K. Keum, K. An, and C. Liang, *Angewandte Chemie - Int. Ed.*, **55**, 8551 (2016).
15. T. W. Kim, K. H. Park, Y. E. Choi, J. Y. Lee, and Y. S. Jung, *J. Mater. Chem. A*, **6**, 840 (2018).
16. Y. Zhao, Y. Yang, and C. A. Wolden, *ACS Appl. Energy Mater.*, **2**, 2246 (2019).
17. W. H. Smith, J. Birnbaum, and C. A. Wolden, *J. Sulfur Chem.*, **42**, 462 (2021).
18. Y. Zhao, W. Smith, and C. A. Wolden, *J. Electrochem. Soc.*, **167**, 070520 (2020).
19. S. Yubuchi, A. Ito, N. Masuzawa, A. Sakuda, A. Hayashi, and M. Tatsumisago, *J. Mater. Chem. A*, **8**, 1947 (2020).
20. L. Zhang, D. Zhang, K. Yang, X. Yan, L. Wang, J. Mi, B. Xu, and Y. Li, *Adv. Sci.*, **3**, 1 (2016).
21. W. Zhao, M. Li, Y. Qi, Y. Tao, Z. Shi, Y. Liu, and J. Cheng, *J. Colloid Interface Sci.*, **586**, 404 (2021).
22. X. Zhou, Z. Zhang, P. Yan, Y. Jiang, H. Wang, and Y. Tang, *Mater. Chem. Phys.*, **244**, 122661 (2020).
23. C. Li, H. Song, C. Mao, H. Peng, and G. Li, *J. of Alloys and Compounds*, **786**, 169 (2019).
24. H. S. Lin and L. Y. Lin, *Electrochim. Acta*, **252**, 235 (2017).
25. H. Lei et al., *Phys. Chem. Chem. Phys.*, **18**, 16436 (2016).
26. A. D. DeAngelis, K. C. Kemp, N. Gaillard, and K. S. Kim, *ACS Appl. Mater. Interfaces*, **8**, 8445 (2016).
27. R. Parize, T. Cossuet, O. Chaix-Pluchery, H. Roussel, E. Appert, and V. Consonni, *Mater. Des.*, **121**, 1 (2017).
28. Y. C. Choi, B. Roose, A. Sadhanala, and H. J. Snaith, *ChemComm*, **51**, 8640 (2015).
29. Y. Cheng, Z. Yao, Q. Zhang, J. Chen, W. Ye, S. Zhou, H. Liu, and M. S. Wang, *Adv. Funct. Mater.*, **2005417**, 1 (2020).
30. J. Zhang, Z. Liu, and Z. Liu, *ACS Appl. Mater. Interfaces*, **8**, 9684 (2016).
31. H. Lei, T. Lin, X. Wang, S. Zhang, Q. Cheng, X. Chen, Z. Tan, and J. Chen, *Mater. Lett.*, **233**, 90 (2018).
32. P. Ge, H. Hou, X. Ji, Z. Huang, S. Li, and L. Huang, *Mater. Chem. Phys.*, **203**, 185 (2018).
33. G. Q. Zhu, P. Liu, H. Y. Miao, J. P. Zhu, X. B. Bian, Y. Liu, B. Chen, and X. B. Wang, *Mater. Res. Bull.*, **43**, 2636 (2008).
34. H. Cao, M. Yu, L. Zhang, Z. Zhang, X. Yan, P. Li, and C. Yu, *J. Mater. Sci. Technol.*, **70**, 168 (2021).
35. H. Wan, J. P. Mwizerwa, F. Han, W. Weng, J. Yang, C. Wang, and X. Yao, *Nano Energy*, **66**, 104109 (2019).
36. G. Lindberg, A. Larsson, M. Råberg, D. Boström, R. Backman, and A. Nordin, *J. Chem. Thermodyn.*, **39**, 44 (2007).
37. G. A. Sehmel, *Cyanide and antimony thermodynamic database for the aqueous species and solids for the EPA-MINTEQ geochemical code*, 224 (1989).
38. Y. Li, L. Wei, R. Zhang, Y. Chen, L. Mei, and J. Jiao, *Nanoscale Res. Lett.*, **8**, 1 (2013).
39. H. Liu, W. Dong, H. Wang, L. Lu, Q. Ruan, Y. S. Tan, R. E. Simpson, and J. K. W. Yang, *Sci. Adv.*, **6**, eabb7171 (2020).
40. N. Tigau, *Cryst. Res.Technol.*, **42**, 281 (2007).
41. G. Ham, S. Shin, J. Park, J. Lee, H. Choi, S. Lee, and H. Jeon, *RSC Adv.*, **6**, 54069 (2016).
42. S. Lee, S. Shin, G. Ham, J. Lee, H. Choi, H. Park, and H. Jeon, *AIP Adv.*, **7**, 025311 (2017).
43. K. Nakamoto, *Infrared and Raman Spectra of Inorganic and Coordination Compounds: Part A: Theory and Applications in Inorganic Chemistry* (Wiley, New York, NY) 6th ed., 1 (2008).
44. M. Kizilyalli, M. Bilgin, and H. M. Kizilyalli, *J. Solid State Chem.*, **85**, 283 (1990).
45. R. H. Arntson, F. W. Dickson, and G. Tunell, *Sci. (New York, N.Y.)*, **153**, 1673 (1966).
46. D. Zhang et al., *Electrochim. Acta*, **259**, 100 (2018).
47. W. Mikenda and A. Preisinger, *Spectrochimica Acta Part A: Molecular Spectroscopy*, **36**, 365 (1980).
48. S. A. Wood, *Geochim. et Cosmochim. Acta*, **53**, 237 (1989).
49. L. Zhou, A. Assoud, Q. Zhang, X. Wu, and L. F. Nazar, *J. American Chem. Soc.*, **141**, 19002 (2019).
50. T. Fuchs, S. P. Culver, P. Till, and W. G. Zeier, *ACS Energy Lett.*, **5**, 146 (2020).
51. J. M. Doux, Y. Yang, D. H. S. Tan, H. Nguyen, E. A. Wu, X. Wang, A. Banerjee, and Y. S. Meng, *J. Mater. Chem. A*, **8**, 5049 (2020).
52. J. Cannarella and C. B. Arnold, *J. Power Sources*, **245**, 745 (2014).
53. T. B. W. B. R. Marvin Cronau, M. Szabo, and C. Konig, *ACS Energy Lett.*, **6**, 3072 (2021).
54. D. Pérez-Coll, E. Sánchez-López, and G. C. Mather, *Solid State Ionics*, **181**, 1033 (2010).
55. K. H. Park, D. Y. Oh, Y. E. Choi, Y. J. Nam, L. Han, J. Y. Kim, H. Xin, F. Lin, S. M. Oh, and Y. S. Jung, *Adv. Mater.*, **28**, 1874 (2016).
56. C. R. Mariappan, C. Yada, F. Rosciano, and B. Roling, *J. Power Sources,*, **196**, 6456 (2011).
57. Y. Gao, N. Li, Y. Wu, W. Yang, and S. H. Bo, *Adv. Energy Mater.*, **11**, 2100325 (2021).